

Kondo screening in a Majorana metal

Received: 17 November 2022

Accepted: 2 November 2023

Published online: 16 November 2023

Check for updates

 S. Lee^{1,9}, Y. S. Choi^{2,9}, S.-H. Do^{3,9}, W. Lee^{1,4}, C. H. Lee⁵, M. Lee⁶, M. Vojta⁷,
 C. N. Wang⁸, H. Luetkens⁸, Z. Guguchia⁸ & K.-Y. Choi² ✉

Kondo impurities provide a nontrivial probe to unravel the character of the excitations of a quantum spin liquid. In the $S = 1/2$ Kitaev model on the honeycomb lattice, Kondo impurities embedded in the spin-liquid host can be screened by itinerant Majorana fermions via gauge-flux binding. Here, we report experimental signatures of metallic-like Kondo screening at intermediate temperatures in the Kitaev honeycomb material α -RuCl₃ with dilute Cr³⁺ ($S = 3/2$) impurities. The static magnetic susceptibility, the muon Knight shift, and the muon spin-relaxation rate all feature logarithmic divergences, a hallmark of a metallic Kondo effect. Concurrently, the linear coefficient of the magnetic specific heat is large in the same temperature regime, indicating the presence of a host Majorana metal. This observation opens new avenues for exploring uncharted Kondo physics in insulating quantum magnets.

When a magnetic impurity is introduced into a metal, conduction electrons interact with the local magnetic moment. At temperatures below the so-called Kondo temperature, the impurity spin becomes effectively screened by the surrounding conduction electrons, creating a many-body entanglement cloud¹. This Kondo effect brings about a reduction in the magnetic moment of the impurity spins and a drastic increase in resistivity. Beyond normal metals, the purview of Kondo physics has expanded into various materials, including quantum dots, graphene, topological insulators, and Weyl semimetals^{2–6}. It is also envisioned that the Kondo effect may occur in quantum spin liquids (QSLs) that constitute highly entangled quantum states harboring fractionalized spinon excitations, an emergent gauge structure, and topological order^{7–16}. In addition, magnetic impurities incorporated into QSLs may be subject to RKKY-type interactions mediated by spinons or gauge fluctuations. In this context, Kondo impurities can act as in-situ probes for QSLs.

A $S = 1/2$ Kitaev model on the honeycomb lattice offers an archetypical platform for exploring unusual Kondo effects: While magnetic insulators often feature bosonic excitations, such as triplons or magnons, which cannot easily screen impurity spins, the fractionalized Kitaev QSL state hosts charge-neutral fermionic excitations, which can

effectively screen impurity spins. At finite temperatures T , itinerant Majorana fermions (MFs) wander around thermally activated π -fluxes ($W_p = -1$)^{17,18}, emulating metallic behavior, whereas the fluxes freeze out at low T , resulting in a Majorana semimetal. When a spin-1/2 impurity is exchange-coupled to a Kitaev spin, a first-order transition takes place at low T as a function of the Kondo coupling between the weak-coupling flux-free phase and the strong-coupling impurity-flux phase. In the latter, each impurity moment binds a gauge flux in the enlarged impurity plaquette, thereby inducing locally metallic behavior of the MFs, in turn leading to Kondo screening^{9–11}.

A conspicuous candidate material for testing the proposed Kitaev Kondo effect is α -RuCl₃^{19,20}, as it is in close proximity to a Kitaev QSL. Its spin Hamiltonian is best described by the K - J - Γ - Γ' model

$$H = \sum_{\langle ij \rangle x} S_i^x \begin{pmatrix} J+K & \Gamma' & \Gamma' \\ \Gamma' & J & \Gamma' \\ \Gamma' & \Gamma' & J \end{pmatrix} S_j^x + \sum_{\langle ij \rangle y} S_i^y \begin{pmatrix} J & \Gamma' & \Gamma' \\ \Gamma' & J+K & \Gamma' \\ \Gamma' & \Gamma' & J \end{pmatrix} S_j^y \\ + \sum_{\langle ij \rangle z} S_i^z \begin{pmatrix} J & \Gamma & \Gamma' \\ \Gamma & J & \Gamma' \\ \Gamma' & \Gamma' & J+K \end{pmatrix} S_j^z$$

¹Center for Artificial Low Dimensional Electronic Systems, Institute for Basic Science, Pohang 37673, Republic of Korea. ²Department of Physics, Sungkyunkwan University, Suwon 16419, Republic of Korea. ³Materials Science and Technology Division, Oak Ridge National Laboratory, Oak Ridge, Tennessee 37831, USA. ⁴Rare Isotope Science Project, Institute for Basic Science, Daejeon 34000, Republic of Korea. ⁵Department of Physics, Chung-Ang University, 84 Heukseok-ro, Seoul 06974, Republic of Korea. ⁶National High Magnetic Field Laboratory, Los Alamos National Laboratory, Los Alamos, New Mexico 87545, USA. ⁷Institut für Theoretische Physik, Technische Universität Dresden, 01062 Dresden, Germany. ⁸Laboratory for Muon Spin Spectroscopy, Paul Scherrer Institute, Villigen PSI 5232, Switzerland. ⁹These authors contributed equally: S. Lee, Y. S. Choi, S.-H. Do. ✉e-mail: choisky99@skku.edu

with dominant Kitaev interaction $K = -5-10$ meV over Heisenberg ($J = -3$ meV) and off-diagonal symmetric exchange interactions $\Gamma = 2-3$ meV and $\Gamma' = 0.1$ meV²¹⁻²³. α -RuCl₃ shows the zigzag magnetic order below $T_N = 6.5$ K, preempting a Kitaev QSL. Although deviations from an ideal Kitaev model occur due to the presence of non-Kitaev terms, many independent experimental techniques suggest that Majorana and gauge degrees of freedom provide a good description of the α -RuCl₃ magnetism at elevated energies and temperatures ($T > J, \Gamma, \Gamma'$)²²⁻²⁵. In addition, α -RuCl₃ benefits from the availability of its isostructural counterpart CrCl₃ (Cr: $3d^3; S = 3/2$)^{26,27}. CrCl₃ is a quasi-two-dimensional ferromagnet (FM) with consecutive FM and AFM orders at $T_C = 17$ K and $T_N = 14$ K, respectively. Taken together, mixed-metal trihalides α -Ru_{1-x}Cr_xCl₃ with random Ru/Cr occupancies²⁸ constitute a suitable model system for studying a Kitaev Kondo problem, gaining a fundamental understanding of $S = 3/2$ impurities embedded in a Kitaev paramagnetic host.

Here, we find several key signatures of metallic Kondo screening in a Kitaev paramagnetic state: logarithmic singularities in magnetic susceptibility, the muon Knight shift, and the muon spin-relaxation rate. Along with these characteristic Kondo signatures, a substantial magnetic contribution to the specific heat, C_m/T , raises the possibility that the observed Kondo screening arises from a Majorana metal host.

Results

Fractionalized spin excitations and structural homogeneity

Figure 1a schematically illustrates the formation of impurity plaquettes ($W_I = -1$; gray polygons) with binding of a gauge flux in the three adjacent plaquettes when $S = 1/2$ magnetic impurities are introduced to a Kitaev spin system. In Fig. 1b, we plot the T - x phase diagram of α -Ru_{1-x}Cr_xCl₃ ($x = 0-0.07$), which reveals a slight reduction in the magnetic ordering temperature to $T_N \approx 5$ K. Additionally, within a Kitaev paramagnetic regime, there is an indication of a weak Kondo coupling, which is a central focus of this study.

We first confirmed the phase purity and composition of α -Ru_{1-x}Cr_xCl₃ through EDX and X-ray diffraction (XRD) analyses, as presented in Supplementary Figs. 1-3. Subsequently, we examine their

structural and magnetic excitations as a function of Cr³⁺ impurity concentration x to clarify the effects of the Cr-for-Ru substitution. Figure 1c shows the Raman spectra obtained at $T = 5$ K in in-plane polarization. For all the investigated $x = 0-0.07$, we observe a broad magnetic continuum (color shadings) with well-defined phonon peaks (Supplementary Fig. 4). In a Kitaev spin liquid, a magnetic Raman scattering process mainly involves the simultaneous creation or annihilation of pairs of MFs²⁹⁻³¹. The observed magnetic Raman response comprises both MF and incoherent magnetic excitations, consistent with previous Raman data^{27,29}. Remarkably, the magnetic continuum varies little with x in its spectral form and intensity (the inset of Fig. 1c). The robustness of fractionalized excitations against Cr³⁺ substitution indicates that a Kitaev paramagnetic state is hardly affected by the insertion of magnetic impurities. Moreover, the Cr³⁺ substitution for Ru³⁺ does not result in any essential changes in the frequency, FWHM, normalized intensity, and the asymmetry parameter $1/|q|$ of the $A_g(1)+B_g(1)$ and $A_g(2)+B_g(2)$ Fano resonance modes (Supplementary Figs. 4 and 5). Additionally, we could not detect any additional phonon peaks within the studied composition range. This observation, in conjunction with the absence of noticeable peak splitting in the single-crystal XRD data (Supplementary Figs. 2 and 3), strongly supports symmetry preservation, excluding the possibility of structural domains or phase segregation. These results suggest that the substituted Cr spins are randomly distributed throughout the lattice, although atomic-scale inhomogeneities cannot be entirely ruled out.

Magnetic impurity effects on a static magnetic response

The Cr³⁺-for-Ru³⁺ substitution modifies the K - J - Γ - Γ' exchange parameters of the mother compound α -RuCl₃ by generating Heisenberg-type interactions on the Cr-Ru bonds. This is because Cr³⁺ ions in the high-spin d^3 $S = 3/2$ configuration are orbitally inactive and, thus, are unable to provide multiple anisotropic and spin-dependent exchange paths required for K - Γ interactions. In the Kitaev paramagnet, this changes the local energetics of the fluxes and also leads to the scattering of the itinerant MFs.

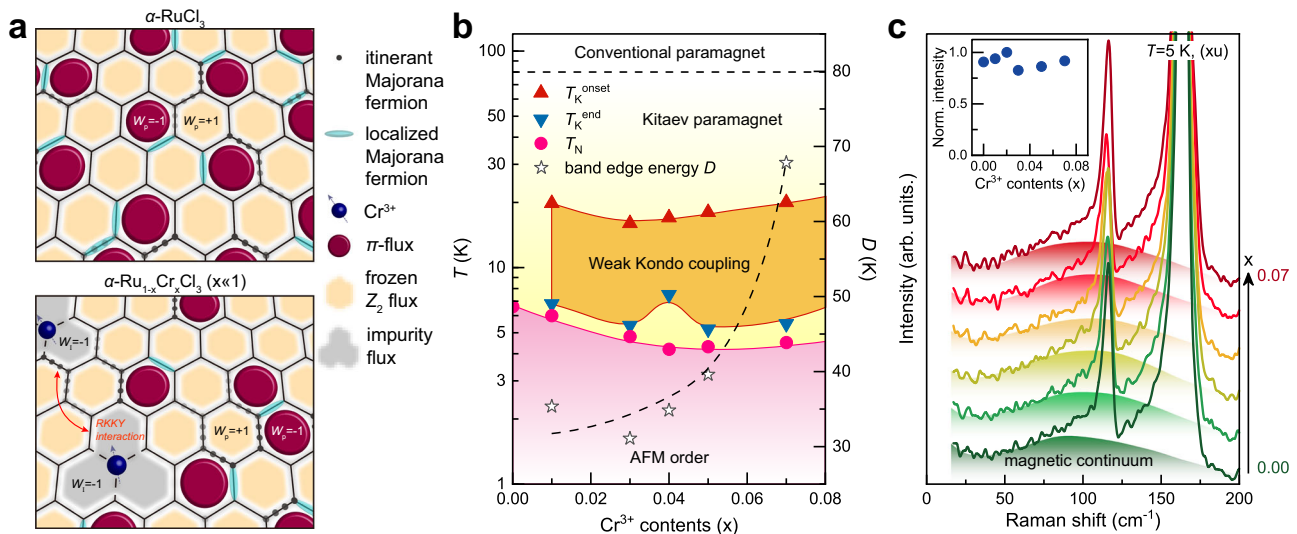


Fig. 1 | Schematic sketch of gauge-flux-driven Kondo screening, x - T phase diagram, and fractionalized excitations of α -Ru_{1-x}Cr_xCl₃. **a** (Top) A Kitaev paramagnetic state consists of coherently propagating Majorana fermions (black dots) and thermally populated π -fluxes ($W_p = -1$) out of the frozen Z_2 gauge fluxes (incarnadine hexagons; $W_p = +1$). (Bottom) Spin- $1/2$ impurities coupled strongly to individual host spins (blue spheres) engender impurity plaquettes ($W_I = -1$; gray polygons) by a gauge flux in the three adjacent plaquettes. In addition, distant magnetic impurities can interact via long-range interactions (orange arrows). **b** T - x

phase diagram of α -Ru_{1-x}Cr_xCl₃ ($x = 0-0.07$). The characteristic temperatures T_K^{onset} , T_K^{end} , and T_N are determined from the dc magnetic susceptibility, specific heat, and μ SR measurements. The band edge energy D is evaluated from the logarithmic fits to the magnetic susceptibility. The black dashed curve is a guide to the eye. AFM stands for antiferromagnetically ordered phase. **c** As-measured Raman spectra at $T = 5$ K. The color shadings denote the broad magnetic continuum. The inset plots the normalized intensity of the magnetic continuum as function of the concentration of the Cr³⁺ ($S = 3/2$) impurities.

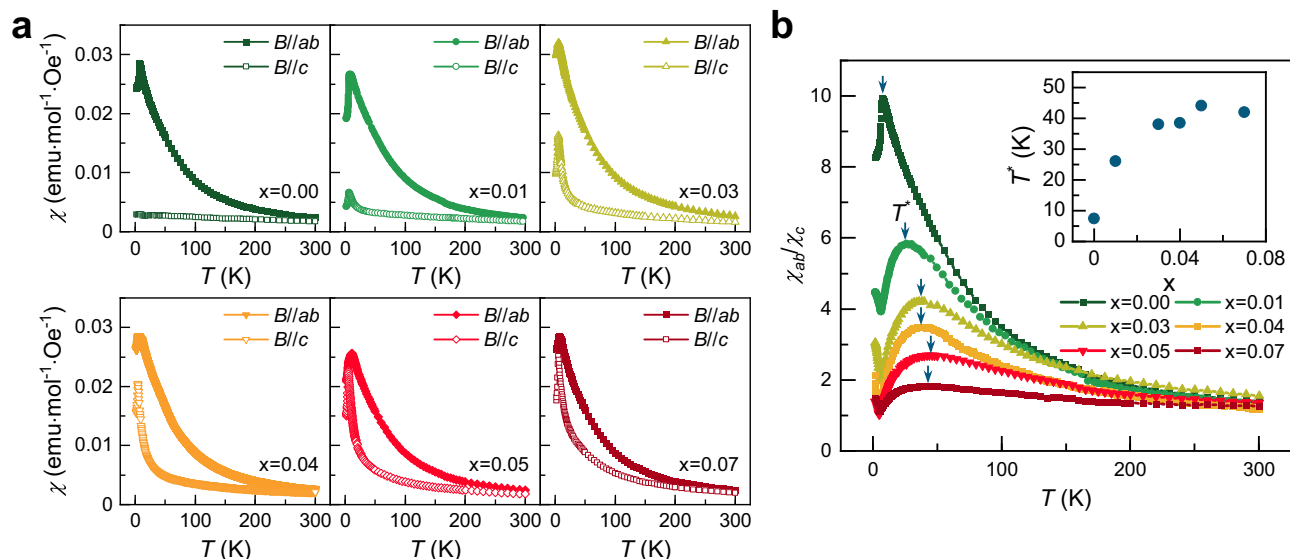


Fig. 2 | Static magnetic susceptibility and magnetic anisotropy as a function of Cr content. **a** Temperature dependence of dc magnetic susceptibility $\chi(T)$ of α - $\text{Ru}_{1-x}\text{Cr}_x\text{Cl}_3$ ($x = 0$ – 0.07) measured in an applied field of $B = 0.1$ T along the ab plane (full symbols) and the c -axis (open symbols). The out-of-plane $\chi_c(T)$ shows a drastic increase with increasing x , rendering the magnetism of α - $\text{Ru}_{1-x}\text{Cr}_x\text{Cl}_3$ isotropic.

b Temperature and composition dependence of the magnetic anisotropy χ_{ab}/χ_c of α - $\text{Ru}_{1-x}\text{Cr}_x\text{Cl}_3$ measured in an applied field of $B = 0.1$ T. An XY-like magnetic anisotropy is systematically reduced with increasing Cr^{3+} concentration. The downward arrows indicate the broad maximum temperature T^* in χ_{ac}/χ_c . The inset plots T^* versus x .

Figure 2a and Supplementary Figs. 6–8 exhibit the static magnetic susceptibilities $\chi(T)$ and magnetization of α - $\text{Ru}_{1-x}\text{Cr}_x\text{Cl}_3$ ($x = 0$ – 0.07) for $B//ab$ and $B//c$, along with corresponding Curie-Weiss fits. The Curie-Weiss behavior is identified in the paramagnetic state above $T = 100$ – 180 K (indicated by the dashed lines in Supplementary Fig. 6), and the Curie-Weiss parameters are summarized in Supplementary Fig. 7. The in-plane $\chi_{ab}(T)$ shows a small variation with x : the Curie-Weiss temperature Θ_{CW}^{ab} and the effective magnetic moment μ_{eff}^{ab} hardly change with increasing Cr^{3+} impurities. The AFM ordering temperature is slightly reduced from $T_N = 6.5$ K at $x = 0$ to 5 K at $x = 0.03$ – 0.07 with no indications of spin-glass behavior down to 2 K. In sharp contrast to $\chi_{ab}(T)$, the out-of-plane $\chi_c(T)$ increases rapidly with increasing x . The large negative Θ_{CW}^c is drastically repressed towards $T = 0$ K and $\mu_{\text{eff}}^c = 3 \mu_B$ is reduced to $2.3 \mu_B$ as x increases up to 0.07 (Supplementary Fig. 7b, c). The drastic impact of the Cr^{3+} impurities on $\chi(T, x)$ is quantified by the magnetic anisotropy $\chi_{ab}(T, x)/\chi_c(T, x)$, as shown in Fig. 2b. With increasing x , the XY-like magnetism becomes more isotropic, signaling that the Cr^{3+} substitution weakens the F - F' terms while enhancing the Heisenberg interaction³². Noteworthy is that a non-monotonic T dependence of χ_{ab}/χ_c features a maximum at about $T^* = 25$ – 40 K above $x = 0.01$ (the vertical arrows in Fig. 2b). The decrease of χ_{ab}/χ_c below T^* alludes to the growth of isotropic magnetic correlations beyond the underlying K - J - F - F' magnetism.

Logarithmic singularities of static magnetic susceptibility

A number of theoretical predictions have been made for impurities in Kitaev QSLs^{9–11,33}, but most of them are valid in the limit of low temperatures only. Here, we are interested in a *finite- T* crossover regime where conventional metallic-like Kondo screening would lead to a logarithmic increase of $\chi(T) \sim \ln(D/T)$, while the flux-binding mechanism in a semimetal would not lead to such logarithmic behavior¹¹.

To test the aforementioned scenarios, we plot $\chi_c(T)$ in Fig. 3a on a semilogarithmic scale, revealing a suggestive logarithmic behavior. To isolate the contribution induced by impurity spins, we present the difference of the static susceptibilities between the pristine and the Cr^{3+} -substituted samples, $\Delta\chi_c(T) = \chi_c(T) - \chi_c(T; x = 0)$ in Fig. 3b and Supplementary Fig. 9. Remarkably, we observe that $\Delta\chi_c(T)$ follows a logarithmic dependence, $\ln(D/T)$, in the temperature interval between T_N

and -20 K. Within this range, we identify two characteristic temperatures, T_K^{onset} and T_K^{end} , which delineate the interval where the logarithmic temperature dependence of $\Delta\chi_c(T)$ appears. In the $T = 30$ – 100 K range, the logarithmic T dependence transits to an approximate power-law dependence $\chi(T) \sim T^{\alpha(T)-1}$ with $\alpha(T) \approx -0.12$ – 0.14 (Supplementary Figs. 9–11), which we interpret as a crossover to the high- T Curie-Weiss-like regime. The deviation from $\alpha = 0$ is attributed to scatterings off of itinerant MFs by Cr^{3+} impurities. The fit parameter D is evaluated to be $D = 23$ – 67 K (the star symbols in Fig. 1b), which is comparable to the strength of the subdominant J - F - F' interactions and roughly agrees with T^* in Fig. 2b. These results suggest that α - $\text{Ru}_{1-x}\text{Cr}_x\text{Cl}_3$ displays Kondo physics different from the flux-driven mechanism of ref. 11. The out-of-plane $\chi_{ab}(T)$ data also hold logarithmic signatures, yet their weak x dependence (Supplementary Fig. 12a) disallows extracting reliable parameters. Further, we note that the Kondo temperature cannot be tracked as the logarithmic behavior is disrupted by the onset of AFM order. Furthermore, we attempted to analyze the $\Delta\chi_c(T)$ data in terms of the equivalent three-channel Kondo model³⁴. We observe a qualitative agreement within the temperature range of $T_N < T < T_K^{\text{onset}}$, but not extending to temperatures $T_K^{\text{onset}} < T$ (Supplementary Fig. 10). Moreover, the derived Kondo temperature T_K is notably lower than T_K^{onset} . This discrepancy is related to the fact that $\Delta\chi_c(T)$ continues to increase upon cooling in the fitting range above T_N (see Supplementary Fig. 10f) and that the Cr impurity in α - $\text{Ru}_{1-x}\text{Cr}_x\text{Cl}_3$ is described by a $S = 3/2$ inequivalent three-channel Kondo model¹¹, as detailed in Supplementary Note 3. In addition, the remaining deviations may originate from inadequate fitting functions and the influence of vison dynamics.

Metallic behavior of Majorana fermions

To probe the Cr^{3+} substitution effect on low-energy excitations, we examine the magnetic specific heat $C_m(T)$ obtained by subtracting lattice contributions from the total specific heat $C_p(T)$ (Supplementary Figs. 11 and 12 and “Methods”). In Fig. 3c, we compare $C_m(T)$ between α - $\text{Ru}_{1-x}\text{Cr}_x\text{Cl}_3$ ($x = 0.04$) and the pristine sample ($x = 0$). $C_m(T)$ of the $x = 0$ sample shows a λ -like peak at $T_N = 6.5$ K, followed by a plateau in the temperature range of $T = 15$ – 50 K and a subsequent increase up to $T_H \sim 100$ K. Upon introducing the Cr^{3+} impurities, two weak anomalies

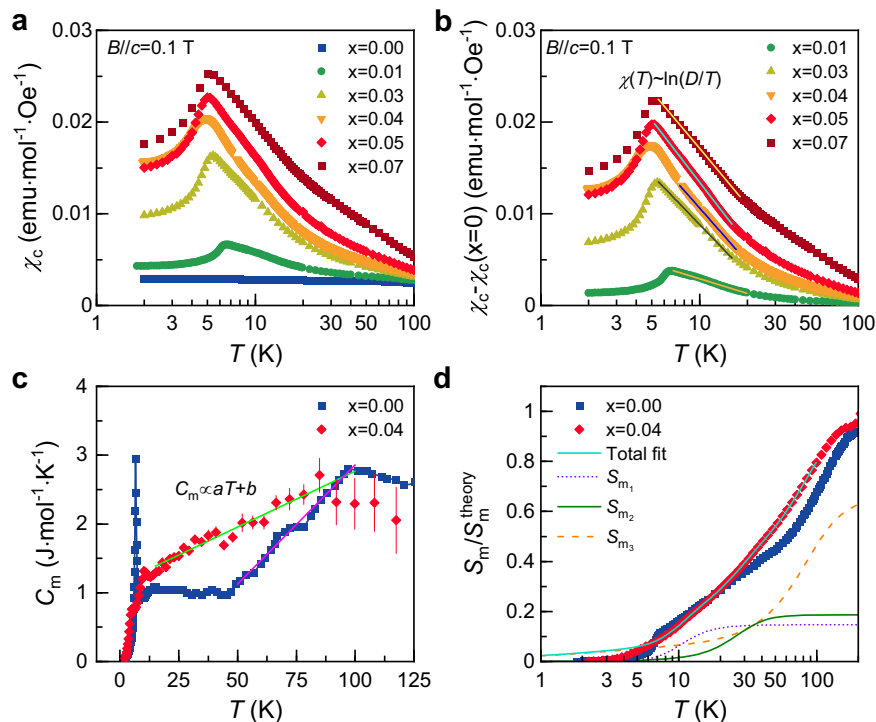


Fig. 3 | Thermodynamic signatures of Kondo screening. **a, b** Temperature dependence of the static magnetic susceptibility $\chi_c(T)$ and the pristine-subtracted $\Delta\chi_c(T) = \chi_c(T) - \chi_c(T; x=0)$ for $\alpha\text{-Ru}_{1-x}\text{Cr}_x\text{Cl}_3$ ($x = 0.01\text{--}0.07$) in an applied field of $B/c = 0.1$ T. The solid lines are fittings to logarithmic divergence $\Delta\chi(T) \sim \ln(D/T)$, where D is the band edge energy. **c** Comparison of the T -dependent magnetic specific heat $C_m(T)$ between $\alpha\text{-Ru}_{1-x}\text{Cr}_x\text{Cl}_3$ ($x = 0.04$) and the pristine material ($x = 0$). $C_m(T)$ is obtained by subtracting a lattice contribution from the total specific heat

(Supplementary Fig. 12). The solid lines indicate a T -linear dependence of $C_m(T)$. The error bars represent one standard deviation of the three repeated specific-heat measurements. **d** Normalized magnetic entropy S_m/S_m^{theory} as a function of temperature evaluated by integrating $C_m(T)/T$ in a semi-log scale. S_m^{theory} is $R\ln 2$ and $0.96R\ln 2 + 0.04R\ln 4$ for $x = 0.00$ and 0.04 , respectively. The solid and dashed lines denote a fit using three phenomenological functions (“Methods”).

appear at $T_{N1} = 4.8$ K and $T_{N2} = 10.4$ K for $x = 0.04$, corresponding to the magnetic ordering of ABC- and AB-type stacking patterns (Supplementary Figs. 11 and 12). As evident from Supplementary Fig. 11b, the addition of 2% magnetic impurities induces a linearly increasing fraction of C_m in the intermediate $T = 13\text{--}50$ K plateau regime for $x = 0$. This trend is enhanced with increasing x up to 0.04. The emergence of a linear T contribution to C_m below T_H is a signature of metallic behavior of the itinerant MFs³⁵. Such effective metallicity arises from the presence of thermally populated π -fluxes ($W_p = -1$), as illustrated in Fig. 1a.

Shown in Fig. 3d is the magnetic entropy $S_m(T) = \int C_m(T)/T dT$. We recall that in an ideal Kitaev system, each half of $S_m(T)$ is released by itinerant and localized MFs³⁶. Unlike the $x = 0$ sample²³, the magnetic entropy of $x = 0.04$ is released in three steps with the weighting factors $\rho_1 = 0.15R\ln 2$, $\rho_2 = 0.19R\ln 2$, $\rho_3 = 0.66R\ln 2$ ($R = \text{ideal gas constant}$) and the crossover temperatures $T_1 = 10.7(3)$ K, $T_2 = 24(4)$ K, and $T_3 = 70(7)$ K (“Methods”). T_1 and T_2 correspond to the end temperatures where the logarithmic behavior of $\chi_c(T)$ appears (Fig. 1b). On the other hand, the power-law dependence $\chi(T) \sim T^{\alpha(T)-1}$ is observed between T_2 and T_3 (Supplementary Fig. 9). We note that one Kondo $S = 3/2$ spin is coupled to the three adjacent $S = 1/2$ sites, leading to flux conservation in the Kitaev QSL only in the joint six-plaquette area surrounding to the impurity^{9–11}. Therefore, 4% Cr^{3+} substitution modifies 24% of the fluxes near the impurities. Qualitatively, the three-step entropy release is consistent with this picture.

Logarithmic singularities of the muon Knight shift and relaxation rate

To shine more light on the Kondo behavior, we carried out muon spin rotation/relaxation (μSR) measurements of $\alpha\text{-Ru}_{1-x}\text{Cr}_x\text{Cl}_3$ ($x = 0.04$) in zero (ZF), longitudinal (LF), weak (wTF), and high (hTF) transverse

fields. The wTF- and ZF- μSR data confirm the two successive magnetic transitions at $T_{N1} = 5$ K and $T_{N2} = 12$ K (Supplementary Figs. 13 and 14), in line with our magnetic and thermodynamic results.

As exhibited in Fig. 4a, the normalized fast Fourier transformed (FFT) amplitudes of the hTF- μSR spectra measured at $T = 15$ K show a Lorentzian shape with intriguing field evolution. Fittings reveal two Lorentzian relaxing cosine components (see Fig. 4b, c): (1) a sharp signal (yellow curve) and (2) a broad signal (green curve). The obtained fitting parameters are plotted in Fig. 4d–g and Supplementary Fig. 15. Given the fact that the field-induced crossover, involving the change of a magnetic domain structure, occurs across $B \sim 1$ T³⁷ (Supplementary Fig. 8), we chose the two representative fields $B_0 = 0.5$ and 3 T for detailed T -dependent studies.

The locally probed intrinsic magnetic susceptibility is reflected in the T -dependent muon Knight shifts $K_f(T)$ and $K_s(T)$. $K_s(T)$ and $K_f(T)$ scale well with $\pm\chi_c(T)$ down to 2 K (Supplementary Fig. 15), indicating that the logarithmic dependence of $\chi(T)$ seen in the $T = T_N - 20$ K range is little affected by extrinsic contributions. Notably, $K_f(T)$ and $K_s(T)$ clearly show distinct temperature dependences. $K_s(T)$ displays a logarithmic dependence $\ln(D/T)$ above 10 K, while $K_f(T)$ shows a power-law behavior T^{-n} (see Fig. 4d, e). The extracted $D = 30.8(6)$ K ($27.9(7)$ K) for $B = 0.5$ T (3 T) is comparable to the value evaluated from the static $\chi_c(T)$ data shown in Fig. 3a, b. Furthermore, based on the relation $\lambda \sim 1/T_1 - A^2 T [\text{Im}\chi(T, \omega)/\omega]_{\omega \rightarrow 0}$, the muon relaxation rate could be expected to follow logarithmic behaviors of $\lambda \sim T[\ln(D/T)]^2$ for a single vacancy or $\lambda \sim 1/T [\ln(D/T)]^2$ for a pair of nearby vacancies on the same sublattice, respectively^{9–11}. We find that only the slow relaxation rate $\lambda_s(T)$ for $B = 3$ T shows a logarithmic T dependence $T[\ln(D/T)]^2$ with $D = 45(1)$ K. On the other hand, $\lambda_f(T)$ follows a power-law behavior $T^{-\alpha}$ with $\alpha = -0.98(1)$ for $B = 3$ T and $\alpha = -2.22(7)$ for $B = 0.5$ T above $T = 8$ K (see Fig. 4f). The concomitant power-law dependence of $\lambda_f(T)$ and $K_f(T)$

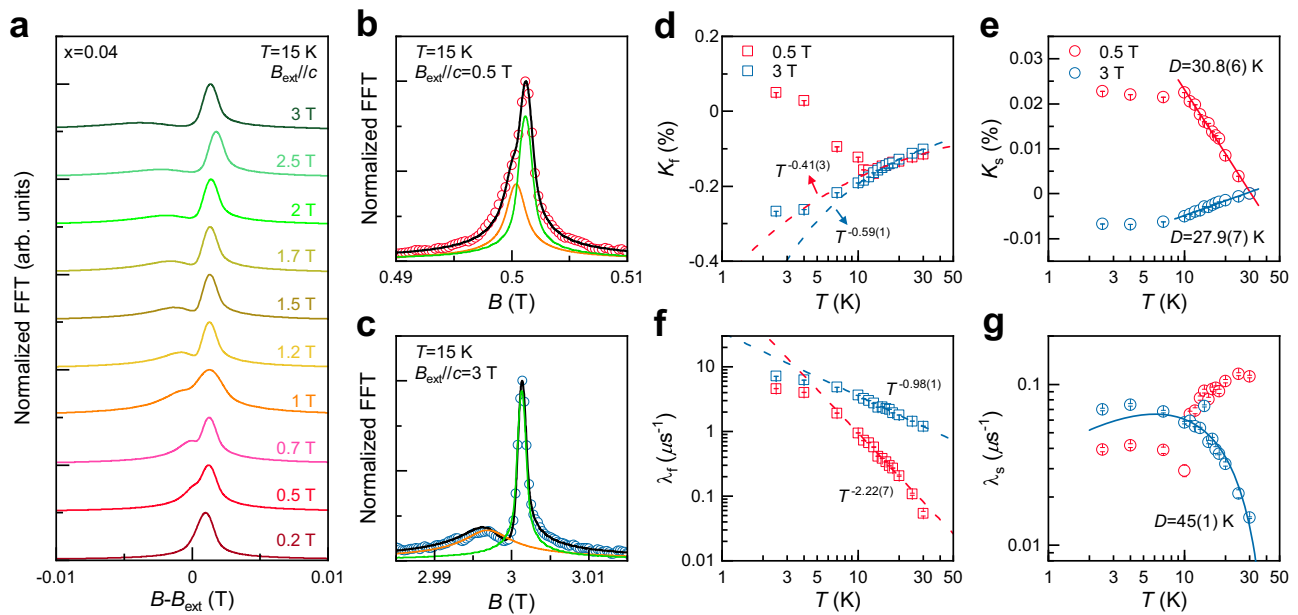


Fig. 4 | High transverse-field μ SR data of α -Ru $_{1-x}$ Cr $_x$ Cl $_3$ ($x = 0.04$). **a** Normalized FFT amplitudes of hTF- μ SR in applied fields of $B_{\text{ext}}/c = 0.2$ – 3 T at $T = 15$ K. The data are vertically shifted for clarity. **b, c** Magnified views of normalized FFT amplitudes at $B_{\text{ext}} = 0.5$ and 3 T. The black solid lines denote the total fitting lines that are a sum of two Lorentzian damped cosines (yellow and green lines). **d, e** Temperature dependence of the muon Knight shift for the fast (K_f) and slow (K_s) relaxing components in applied fields of $B_{\text{ext}}/c = 0.5$ and 3 T. $K_f(T)$ is described by power-law behaviors $K_f \sim T^{-n}$ (dashed lines), which deviates below $T_{N2} = 12$ K, while $K_s(T)$

exhibits a logarithmic dependence $K_s \sim \ln(D/T)$ (solid lines) predicted for a singlet vortex case above 10 K. Error bars represent one standard deviation. **f, g** Muon spin-relaxation rates for the fast (λ_f) and slow (λ_s) component as a function of temperature on a double logarithmic scale. $\lambda_f(T)$ displays a power-law down to T_{N2} (dashed lines), similar to K_f . On the other hand, $\lambda_s(T)$ at $B_{\text{ext}} = 3$ T is well described by a logarithmic dependence $\lambda_s \sim 1/T_1 - T[\ln(D/T)]^2$ (solid lines). Error bars of the muon Knight shift and the relaxation rate represent one standard deviation of the fit parameters.

suggests that the fast component stems from correlated spins pertinent to defects and bond disorders, which inevitably occur due to stacking faults and local strains induced by the Cr $^{3+}$ -for-Ru $^{3+}$ substitution. Actually, the static magnetic susceptibility follows an approximate power law $\chi(T) \sim T^{\alpha(T)-1}$ in the elevated temperatures of $T = 30$ – 100 K.

Discussion

Combining specific heat, magnetic susceptibility, and μ SR probes, we find that mixed-metal trihalides α -Ru $_{1-x}$ Cr $_x$ Cl $_3$ offer a promising arena for exploring a Kitaev Kondo problem. The magnetism of α -Ru $_{1-x}$ Cr $_x$ Cl $_3$ is modeled by the K - J - F - F' spin Hamiltonian 32 , where the strength of J relative to F - F' increases with x . Our findings reveal several key points.

First, we observe that the Cr $^{3+}$ substitution exerts no significant impact on fractionalized excitations at intermediate T (Fig. 1c and Supplementary Fig. 4) despite the Heisenberg-type interaction $J_{\text{Ru-Cr}}$ perturbs the original K - J - F - F' exchange interactions. Second, as evident from the rapid suppression of XY-like magnetic anisotropy in Fig. 2b, the inclusion of the spin- $\frac{3}{2}$ impurities diminishes the F - F' terms, while augmenting the isotropic Heisenberg interaction. Third, $C_m(T)$ and $S_m(T)$, tracking thermal fractionalization of spins into itinerant MFs and Z_2 fluxes, demonstrate that the addition of magnetic impurities expands the Kitaev paramagnetic state down to T_N , which is much lower than ~ 50 K of α -RuCl $_3$. The sizeable linear term in C_m , a hallmark of the metallic density of states, negates a paramagnon scenario. This expanded Majorana-metal regime can be rationalized by noting that the impurities both increase the fluctuations of the gauge fluxes and, at the same time, scatter the itinerant MFs, thereby inducing low-energy Majorana states. Fourth, both static and dynamic magnetic probes commonly feature logarithmic singularities of the conventional Kondo effect. Finally, the three-step release of $S_m(T)$, the three-step evolution of $\chi(T)$, and the magnetic anisotropy (χ_{ab}/χ_c) anomaly at $T \approx 25$ – 40 K

equivocally evidence the emergence of magnetic correlations induced by a few percentages of magnetic impurities.

This together with the large Kondo energy of ~ 30 K suggests that the scenario 11 of low- T gauge-flux-driven Kondo screening in a Majorana semimetal is not applicable to α -Ru $_{1-x}$ Cr $_x$ Cl $_3$. Instead, at elevated temperatures, a strongly fluctuating flux (or vison) background produces a Majorana metal host. In this situation, no explicit binding of fluxes to impurities is required for Kondo screening. Rather, the global presence of thermally excited gauge fluxes provides a natural mechanism for a metallic Kondo effect with logarithmic signatures, here for $S = 3/2$ moments with three inequivalent screening channels 11 , here for $S = 3/2$ moments with three screening channels. At larger x , this Kondo physics will compete against the fluctuation-mediated inter-impurity interactions. We recall that the Kondo effect in a magnetic insulator has recently been reported in the Zn-brochantite ZnCu $_3$ (OH) $_6$ SO $_4$, a Kagome antiferromagnet that holds a proximate QSL 8 . In this case, magnetic impurities originating from Cu-Zn intersite disorders act as Kondo spins that may be screened by spinon-spinon interactions, but the precise mechanism has not been clarified. Thanks to its analytical solvability, however, an impurity-doped Kitaev system enables the exploration of uncharted territory including multi-channel Kondo physics and its interplay with gauge fluctuations.

To conclude, we have showcased metallic-like Kondo behavior in the Kitaev candidate material α -Ru $_{1-x}$ Cr $_x$ Cl $_3$ containing $S = 3/2$ magnetic impurities, demonstrating the presence of a host Majorana metal. Multiple Kondo impurities and their interplay may bring about a new species of Kondo and ordering phenomena. Extending the present phenomena to low temperatures in a material without magnetic ordering would give access to the regime of flux binding by impurities 11 , then raising the prospect of braiding impurity fluxes via impurity manipulation toward the implementation of quantum computation 17,18 .

Methods

Sample preparation

Single crystals of α -Ru $_{1-x}$ Cr $_x$ Cl $_3$ ($x = 0-0.07$) were synthesized by a vacuum sublimation method. A commercial compound of RuCl $_3$ (Alfa Aesar) was ground and dried in a quartz tube under vacuum until it was completely dehydrated. The resulting powder was then sealed in an evacuated quartz ampule, which was placed in a temperature gradient furnace. The ampule was heated at 1080 °C for 24 h and then slowly cooled down to 600 °C at a rate of 2 °C/h. The obtained single crystals have typical sizes of about 5 × 5 × 1 mm 3 with a shiny black surface.

Structural and thermodynamic measurements

The crystal structure of α -Ru $_{1-x}$ Cr $_x$ Cl $_3$ was determined by X-ray diffraction measurements using Cu K α radiation (the Bruker D8-advance model). The phase purity and stoichiometry of the single crystals were confirmed by energy dispersive X-ray spectroscopy (EDX). The actual Ru:Cr ratio was evaluated by scanning a dozen spots of 50 μ m size (Supplementary Fig. 1). The standard deviation from the mean value is evaluated to be -1 mol% Cr for all crystals. We measured dc magnetic susceptibility and magnetization with a SQUID (Quantum Design MPMS) and Physical Property Measurements System (Quantum Design PPMS Dynacool) for $B//ab$ and $B//c$ in the temperature range $T = 2-300$ K. High-field magnetization measurements were conducted at the Dresden High Magnetic Field Laboratory with a pulsed-field magnet (25 ms duration) using an induction method with a pickup coil device at $T = 2$ K. Specific heat experiments were carried out under applied fields of $B//c = 0, 0.5,$ and 3 T in the temperature range of $T = 2-200$ K with a thermal relaxation method using a commercial set-up of Physical Property Measurements System.

The magnetic specific heat of α -Ru $_{1-x}$ Cr $_x$ Cl $_3$ was obtained by subtracting the specific heat of the isostructural nonmagnetic counterpart ScCl $_3$. Using the Bouvier method³⁸, we scaled the specific heat data of ScCl $_3$ by the molecular mass and Debye temperature and then used this scaled specific heat data to evaluate the magnetic specific heat of the Cr-doped RuCl $_3$. In doing that, we assumed that the Debye temperature does not vary significantly with the small Cr concentration (Supplementary Figs. 11 and 12). The magnetic specific heat was fitted using a sum of two phenomenological functions³⁹, $S_m = \sum_{i=1,3} S_{m_i} = \sum_{i=1,3} \frac{\rho_i/2}{1 + \exp\left[\frac{\beta_i + \gamma_i T_i/T}{1 + T_i/T} \ln\left(\frac{T_i}{T}\right)\right]}$. Here, ρ_i is the weighting factor with a scaled constraint of $\rho_1 + \rho_2 + \rho_3 = 2.14$ and T_i is the cross-over temperature. β_i and γ_i are the power exponents at high and low temperatures, respectively. The fitting parameters are evaluated to be $\rho_1 = 0.32(1)$, $\beta_1 = 2.9(2)$, $\gamma_1 = 5.18(9)$, $T_1 = 10.7(3)$ K, $\rho_2 = 0.41(5)$, $\beta_2 = 5.13(7)$, $\gamma_2 = 1.6(3)$, $T_2 = 24(4)$ K, $\rho_3 = 1.41(3)$, $\beta_3 = 3.88(9)$, $\gamma_3 = 0.7(2)$, and $T_3 = 70(7)$ K.

Raman scattering

Raman scattering experiments were conducted in backscattering geometry with the excitation line $\lambda = 532$ nm of the DPSS SLM laser. The Raman scattering spectra were collected using a micro-Raman spectrometer (XperRam200VN, NanoBase) equipped with an air-cooled charge-coupled device (Andor iVac Camera). We employed a notch filter to reject Rayleigh scattering at low frequencies below 15 cm $^{-1}$. The laser beam with $P = 80$ μ W was focused on a few-micrometer-diameter spot on the surface of the crystals using a $\times 40$ magnification microscope objectives. The samples were mounted onto a 4 He continuous flow cryostat by varying a temperature $T = 4-300$ K.

Phonon excitations below 200 cm $^{-1}$ were fitted using an asymmetric Fano profile $I(\omega) = I_0 \frac{(q + \epsilon)^2}{(1 + \epsilon^2)}$, where $\epsilon = (\omega - \omega_0)/\Gamma$ and Γ is the full width at half maximum (FWHM) in case of strong coupling between spin and lattice degree of freedom. $1/|q|$ provides a measure of the

coupling strength between a magnetic continuum and optical phonons or conveys information about Majorana excitations.

Muon spin relaxation/rotation

Muon spin-relaxation/rotation (μ SR) measurements were conducted on the GPS⁴⁰ and the HAL-9500 spectrometers at the Paul Scherrer Institute (Villigen, Switzerland). For the GPS spectrometer measurements, a mosaic of a -axis coaligned single crystals (~ 0.5 g) was packed in an aluminum foil and attached to a sample holder. The Veto mode was activated to minimize the background signal. ZF- and TF- μ SR experiments on the GPS spectrometer were performed in the spin-rotated mode, where the initial muon spins were rotated by 45° from the muon momentum direction (c -axis). It should be noted that α -RuCl $_3$ shows anisotropic 2D XY-like magnetism, resulting in weaker spin correlations along the c -axis compared to those in the ab -plane. This makes it difficult to detect changes in the muon spin relaxation when the muon spins are directed along the c -axis. To minimize the contribution of spin correlations along the c -axis, up and down detectors were utilized in this spin-rotated mode. On the other hand, LF- μ SR measurements on the GPS spectrometer were carried out in the longitudinal mode, where the initial muon spins were parallel to the c -axis. For the HAL-9500 experiments, a single piece of large single crystal (8 × 8 × 1 mm 3 , -150 mg) was wrapped with a Ag foil and attached to a silver sample holder using GE varnish. All the measurements were carried out in the spin-rotated mode that the initial muon spins were rotated by 90° and lie in the ab -plane. The transverse fields ($B = 0-3$ T) were applied along the c -axis.

All obtained μ SR spectra were analyzed with the software package MUSRFIT with GPU acceleration support⁴¹⁻⁴⁴. The weak transverse-field (wTF) μ SR spectra were fitted with a sum of an exponentially decaying cosine and a simple exponential function, $P_z(t) = f \cos(2\pi\nu_s t + \phi_s) \exp(-\lambda_s t) + (1-f) \exp(-\lambda_f t)$, where f is the slow relaxing fraction, ν_s is the muon spin precession frequency, ϕ_s is a phase, and λ_s (λ_f) is the muon spin-relaxation rate for the slow (fast) decaying component.

The zero-field (ZF) μ SR data were well described by a sum of the Gaussian-broadened Gaussian (GbG) function with a simple exponential decay and a simple exponential function,

$$P_z(t) = f P_{\text{GbG}}(t; \Delta_0, W) \exp(-\lambda_s t) + (1-f) \exp(-\lambda_f t)$$

The GbG depolarization function is defined as a convolution of the Gaussian Kubo-Toyabe function, characterizing a broader field distribution than the Gaussian field distribution,

$$P_{\text{GbG}}(t) = a + (1-a) \left(\frac{1}{1 + R^2 \Delta_0^2 t^2} \right)^{3/2} \left(1 - \frac{\Delta_0^2 t^2}{1 + R^2 \Delta_0^2 t^2} \right) \exp \left[-\frac{\Delta_0^2 t^2}{2(1 + R^2 \Delta_0^2 t^2)} \right]$$

Here, a is the tail fraction, $1-a$ is the damped relaxing fraction, Δ_0 is the mean value, W is the Gaussian width, and $R (=W/\Delta_0)$ is the relative Gaussian width of the Gaussian distribution, respectively. The GbG function well accounts for inhomogeneous static magnetic moments with short-range correlations⁴⁵⁻⁴⁸. Note that the ZF- μ SR results of the nonmagnetic Ir $^{3+}$ ($J_{\text{eff}} = 0$) substituted α -Ru $_{1-x}$ Ir $_x$ Cl $_3$ are also well described by the identical model, suggesting the similar effects of magnetic (Cr $^{3+}$, $S = 3/2$) and nonmagnetic impurities on the Kitaev quantum spin system α -RuCl $_3$ ⁴⁸.

The longitudinal-field (LF) μ SR data were fitted by a sum of the static and the dynamic Gaussian Kubo-Toyabe functions in longitudinal fields,

$$P_z(t) = f P_{\text{SGKT}}(t, \Delta_s, B_{\text{LF}}) + (1-f) P_{\text{DGKT}}(t, \Delta_f, \Gamma_f, B_{\text{LF}}),$$

where, P_{SGKT} (P_{DGKT}) are the dynamic (static) Gaussian Kubo-Toyabe function, F_f is the local field fluctuation rate, B_{LF} is the applied LF, and Δ_f (Δ_s) is the local-field width at the muon interstitial sites. The internal field is evaluated to be $\langle B_{\text{loc}} \rangle \sim 16.88$ mT (Supplementary Fig. 16).

High transverse-field (hTF) μSR results were analyzed by the single histogram fit method. The positron histogram of the i -th detector $N_i(t)$ is given by $N_i(t) = N_{0,i} e^{-t/\tau_\mu} [1 + A_{0,i} P_i(t)] + N_{\text{bkg},i}$, where $N_{0,i}$ is the total muon decay events at $t = 0$, τ_μ is the mean lifetime of the muon ($\sim 2.2 \mu\text{s}$), $A_{0,i}$ is the intrinsic asymmetry of the i -th detector, $P_i(t)$ is the time-dependent muon spin polarization, and $N_{\text{bkg},i}$ is background events. We employed a sum of two Gaussian damped cosines for fittings, $P_i(t) = f \cos(2\pi\nu_s t + \phi_s) \exp[-\lambda_s t] + (1-f) \cos(2\pi\nu_f t + \phi_f) \exp[-\lambda_f t]$, where f is the relaxing fraction.

In general, to calculate the Knight shift, the narrow peak arising from the Ag sample holder is used as an internal reference. However, as shown in Fig. 4, the FFT spectra of $\alpha\text{-Ru}_{1-x}\text{Cr}_x\text{Cl}_3$ ($x = 0.04$) display the overlap of the background and the intrinsic sample signals at slightly higher than the applied field B_{ext} . Therefore, we used the peak position of the sharp signal at $T = 30$ K that was obtained from the analysis as the reference field for evaluating the Knight shift.

Data availability

The magnetic susceptibility, specific heat, and Raman data generated in this study are provided in the Supplementary Information/Source Data file. The μSR data used in this study are available in the PSI database [<http://musruser.psi.ch/cgi-bin/SearchDB.cgi>]. Source data are provided with this paper.

References

- Kondo, J. Resistance minimum in dilute magnetic alloys. *Prog. Theor. Phys.* **32**, 37–49 (1964).
- Cronenwett, S. M., Oosterkamp, T. H. & Kouwenhoven, L. P. A tunable Kondo effect in quantum dots. *Science* **281**, 540–544 (1998).
- Cha, J. J. et al. Magnetic doping and Kondo effect in Bi_2Se_3 nanoribbons. *Nano Lett.* **10**, 1076–1081 (2010).
- Chen, J.-H., Li, L., Cullen, W. G., Williams, E. D. & Fuhrer, M. S. Tunable Kondo effect in graphene with defects. *Nat. Phys.* **7**, 535–538 (2011).
- Béri, B. & Cooper, N. R. Topological Kondo effect with Majorana fermions. *Phys. Rev. Lett.* **109**, 156803 (2012).
- Dzsaber, S. et al. Kondo insulator to semimetal transformation tuned by spin-orbit coupling. *Phys. Rev. Lett.* **118**, 246601 (2017).
- Savary, L. & Balents, L. Quantum spin liquids: a review. *Rep. Prog. Phys.* **80**, 016502 (2016).
- Gomilšek, M. et al. Kondo screening in a charge-insulating spinon metal. *Nat. Phys.* **15**, 754 (2019).
- Willans, A. J., Chalker, J. T. & Moessner, R. Disorder in a quantum spin liquid: flux binding and local moment formation. *Phys. Rev. Lett.* **104**, 237203 (2010).
- Dhochak, K., Shankar, R. & Tripathi, V. Magnetic impurities in the honeycomb Kitaev model. *Phys. Rev. Lett.* **105**, 117201 (2010).
- Vojta, M., Mitchell, A. K. & Zschocke, F. Kondo impurities in the Kitaev spin liquid: numerical renormalization group solution and gauge-flux-driven screening. *Phys. Rev. Lett.* **117**, 037202 (2016).
- Das, S. D., Dhochak, K. & Tripathi, V. Kondo route to spin inhomogeneities in the honeycomb Kitaev model. *Phys. Rev. B* **94**, 024411 (2016).
- Wang, R., Wang, Y., Zhao, Y. X. & Wang, B. Emergent Kondo behavior from gauge fluctuations in spin liquids. *Phys. Rev. Lett.* **127**, 237202 (2021).
- Khaliullin, G. & Fulde, P. Magnetic impurity in a system of correlated electrons. *Phys. Rev. B* **52**, 9514–9519 (1995).
- Kolezhuk, A., Sachdev, S., Biswas, R. R. & Chen, P. Theory of quantum impurities in spin liquids. *Phys. Rev. B* **74**, 165114 (2006).
- Ribeiro, P. & Lee, P. A. Magnetic impurity in a U(1) spin liquid with a spinon Fermi surface. *Phys. Rev. B* **83**, 235119 (2011).
- Kitaev, A. Anyons in an exactly solved model and beyond. *Ann. Phys.* **321**, 2–111 (2006).
- Baskaran, G., Mandal, S. & Shankar, R. Exact results for spin dynamics and fractionalization in the Kitaev model. *Phys. Rev. Lett.* **98**, 247201 (2007).
- Plumb, K. W. et al. $\alpha\text{-RuCl}_3$: a spin-orbit assisted Mott insulator on a honeycomb lattice. *Phys. Rev. B* **90**, 041112 (2014).
- Banerjee, A. et al. Proximate Kitaev quantum spin liquid behaviour in a honeycomb magnet. *Nat. Mater.* **15**, 733–740 (2016).
- Koitzsch, A. et al. J_{eff} description of the honeycomb Mott insulator $\alpha\text{-RuCl}_3$. *Phys. Rev. Lett.* **117**, 126403 (2016).
- Hermanns, M., Kimchi, I. & Knolle, J. Physics of the Kitaev model: fractionalization, dynamical correlations, and material connections. *Annu. Rev. Condens. Matter Phys.* **9**, 17–33 (2017).
- Takagi, H., Takayama, T., Jackeli, G., Khaliullin, G. & Nagler, S. E. Concept and realization of Kitaev quantum spin liquids. *Nat. Rev. Phys.* **1**, 264–280 (2019).
- Do, S.-H. et al. Majorana fermions in the Kitaev quantum spin system $\alpha\text{-RuCl}_3$. *Nat. Phys.* **13**, 1079–1084 (2017).
- Li, H. et al. Identification of magnetic interactions and high-field quantum spin liquid in $\alpha\text{-RuCl}_3$. *Nat. Commun.* **12**, 4007 (2021).
- Cable, J. W., Wilkinson, M. K. & Wollan, E. O. Neutron diffraction investigation of antiferromagnetism in CrCl_3 . *J. Phys. Chem. Solids* **19**, 29–34 (1961).
- Glamazda, A., Lemmens, P., Do, S.-H., Kwon, Y. S. & Choi, K.-Y. Relation between Kitaev magnetism and structure in $\alpha\text{-RuCl}_3$. *Phys. Rev. B* **95**, 174429 (2017).
- Bastien, G. et al. Spin-glass state and reversed magnetic anisotropy induced by Cr doping in the Kitaev magnet $\alpha\text{-RuCl}_3$. *Phys. Rev. B* **99**, 214410 (2019).
- Nasu, J., Knolle, J., Kovrizhin, D. L., Motome, Y. & Moessner, R. Fermionic response from fractionalization in an insulating two-dimensional magnet. *Nat. Phys.* **12**, 912–915 (2016).
- Glamazda, A., Lemmens, P., Do, S. H., Choi, Y. S. & Choi, K. Y. Raman spectroscopic signature of fractionalized excitations in the harmonic-honeycomb iridates β - and $\gamma\text{-Li}_2\text{IrO}_3$. *Nat. Commun.* **7**, 12286 (2016).
- Wulferding, D., Choi, Y., Lee, W. & Choi, K.-Y. Raman spectroscopic diagnostic of quantum spin liquids. *J. Phys. Condens. Matter* **32**, 043001 (2019).
- Chaloupka, J. & Khaliullin, G. Magnetic anisotropy in the Kitaev model systems Na_2IrO_3 and RuCl_3 . *Phys. Rev. B* **94**, 064435 (2016).
- Sanyal, S., Damle, K., Chalker, J. T. & Moessner, R. Emergent moments and random singlet physics in a Majorana spin liquid. *Phys. Rev. Lett.* **127**, 127201 (2021).
- Schlottmann, P. & Sacramento, P. D. Multichannel Kondo problem and some applications. *Adv. Phys.* **42**, 641 (1993).
- Han, J.-H. et al. Weak-coupling to strong-coupling quantum criticality crossover in a Kitaev quantum spin liquid liquid $\alpha\text{-RuCl}_3$. *NPJ Quantum Mater.* **8**, 33 (2023).
- Nasu, J., Udagawa, M. & Motome, Y. Thermal fractionalization of quantum spins in a Kitaev model: temperature-linear specific heat and coherent transport of Majorana fermions. *Phys. Rev. B* **92**, 115122 (2015).
- Sears, J. A., Zhao, Y., Xu, Z., Lynn, J. W. & Kim, Y.-J. Phase diagram of $\alpha\text{-RuCl}_3$ in an in-plane magnetic field. *Phys. Rev. B* **95**, 180411 (2017).
- Bouvier, M., Lethuillier, P. & Schmitt, D. Specific heat in some gadolinium compounds. I. Experimental. *Phys. Rev. B* **43**, 13137 (1991).
- Yamaji, Y. et al. Clues and criteria for designing a Kitaev spin liquid revealed by thermal and spin excitations of the honeycomb iridate Na_2IrO_3 . *Phys. Rev. B* **93**, 174425 (2016).

40. Amato, A. et al. The new versatile general purpose surface-muon instrument (GPS) based on silicon photomultipliers for μ SR measurements on a continuous-wave beam. *Rev. Sci. Instrum.* **88**, 093301 (2017).
41. Suter, A. & Wojek, B. M. musfit: a free platform-independent framework for μ SR data analysis. *Phys. Procedia* **30**, 69–73 (2012).
42. Adelmann, A., Locans, U. & Suter, A. The Dynamic Kernel Scheduler—Part 1. *Comput. Phys. Commun.* **207**, 83–90 (2016).
43. Locans, U. et al. Real-time computation of parameter fitting and image reconstruction using graphical processing units. *Comput. Phys. Commun.* **215**, 71–80 (2017).
44. Locans, U. & Suter, A. MUSRFIT—real time parameter fitting using GPUs. *JPS Conf. Proc.* **21**, 011051 (2018).
45. Noakes, D. R. & Kalvius, G. M. Anomalous zero-field muon spin relaxation in highly disordered magnets. *Phys. Rev. B* **56**, 2352–2355 (1997).
46. Dally, R. et al. Short-range correlations in the magnetic ground state of $\text{Na}_4\text{Ir}_3\text{O}_8$. *Phys. Rev. Lett.* **113**, 247601 (2014).
47. Hodges, J. A. et al. First-order transition in the spin dynamics of geometrically frustrated $\text{Yb}_2\text{Ti}_2\text{O}_7$. *Phys. Rev. Lett.* **88**, 077204 (2002).
48. Do, S.-H. et al. Short-range quasistatic order and critical spin correlations in $\alpha\text{-Ru}_{1-x}\text{Ir}_x\text{Cl}_3$. *Phys. Rev. B* **98**, 014407 (2018).

Acknowledgements

We gratefully acknowledge R. Scheuermann for assistance with the experiment and critical reading of our manuscript. The work at CAU and SKKU was supported by the National Research Foundation (NRF) of Korea (Grant no. RS-2023-00209121, 2020R1A5A1016518). A portion of this work was performed at the National High Magnetic Field Laboratory, which is supported by the National Science Foundation Cooperative Agreement No. DMR-1644779 and the State of Florida and the U.S. Department of Energy. This material is based upon work supported by the U.S. Department of Energy, Office of Science, National Quantum Information Science Research Centers. This work was supported by the Rare Isotope Science Project of the Institute for Basic Science funded by the Ministry of Science and ICT and NRF of Korea (2013M7A1A1075764). The research of M.V. was supported by the Deutsche Forschungsgemeinschaft (DFG) via the Cluster of Excellence ct.qmat (EXC 2147, project id 390858490) and via SFB 1143 (project id 247310070). Z.G. acknowledges support from the Swiss National Science Foundation (SNSF) through SNSF Starting Grant (No. TMSGI2_211750). The research of Y.C. was supported by the Sung-KyunKwan University and the BK21 FOUR (Graduate School Innovation) funded by the Ministry of Education (MOE, Korea) and NRF of Korea.

Author contributions

K.-Y.C. designed and conceived the project. K.-Y.C. and S.L. planned the experiments. Y.S.C., S.-H.D., and C.H.L. synthesized the samples and characterized structural properties. S.L., Y.S.C., S.-H.D., and M.L. conducted magnetic property measurements. Y.S.C. performed the Raman scattering experiments and analyzed the Raman data. S.L., C.W., H.L., and Z.G. carried out μ SR experiments, and S.L. and W.L. analyzed the data. Data analysis and figure preparation were performed by S.L., M.V., and K.-Y.C. The manuscript was written through the contributions of all authors.

Competing interests

The authors declare no competing interests.

Additional information

Supplementary information The online version contains supplementary material available at <https://doi.org/10.1038/s41467-023-43185-3>.

Correspondence and requests for materials should be addressed to K.-Y. Choi.

Peer review information *Nature Communications* thanks the anonymous reviewers for their contribution to the peer review of this work. A peer review file is available.

Reprints and permissions information is available at <http://www.nature.com/reprints>

Publisher's note Springer Nature remains neutral with regard to jurisdictional claims in published maps and institutional affiliations.

Open Access This article is licensed under a Creative Commons Attribution 4.0 International License, which permits use, sharing, adaptation, distribution and reproduction in any medium or format, as long as you give appropriate credit to the original author(s) and the source, provide a link to the Creative Commons licence, and indicate if changes were made. The images or other third party material in this article are included in the article's Creative Commons licence, unless indicated otherwise in a credit line to the material. If material is not included in the article's Creative Commons licence and your intended use is not permitted by statutory regulation or exceeds the permitted use, you will need to obtain permission directly from the copyright holder. To view a copy of this licence, visit <http://creativecommons.org/licenses/by/4.0/>.

© The Author(s) 2023